EES Catalysis

PAPER

View Article Online
View Journal | View Issue

Cite this: *EES Catal.*, 2025, 3, 1075

Ni and Mo atom pairs as single sites on N-doped graphitic carbon for urea formation by simultaneous CO_2 and NO_3^- reduction with pulsed electrocatalysis†

Jiajun Hu,[a] Silvio Osella,[b] Josep Albero *[a] and Hermenegildo García *[a]

Received 20th February 2025,
Accepted 6th May 2025

DOI: 10.1039/d5ey00056d

rsc.li/eescatalysis

Ni and Mo atom pairs as single sites supported on N-doped graphitic carbon was prepared by pyrolysis of a mixture of $Ni(NO_3)_2$, $(NH_4)_6Mo_7O_{24}$, glucose, and melamine at 800 °C and subsequent washing with HCl. Coulombic association between Ni^{2+} and $Mo_7O_{24}^{6-}$ is key for the formation of the Ni–Mo pairs (distance: 0.23 nm), whose presence was determined by atomic resolution aberration-corrected STEM and EXAFS. The dual NiMo-DASC exhibits better performance for urea formation by simultaneous electrochemical CO_2 and NO_3^- reduction reactions than the Ni- or Mo-single atom catalysts on N-doped graphitic carbon prepared analogously at similar total metal loadings and surface areas. Using pulsed electrochemical reduction of −0.5 V *vs.* RHE for NO_3RR and −0.7 V *vs.* RHE to promote CO_2RR, urea was formed with a faradaic efficiency of 31.8% and a yield of 11.3 mmol h^{-1} g^{-1}. The sources of C and N were confirmed by isotopic ^{13}C and ^{15}N labelling experiments using NMR spectroscopy. *In situ* surface enhanced IR spectroscopy shows the appearance of adsorbed *CO (1937 cm^{-1}), *NH species (1636 cm^{-1}) and C–N (1597 cm^{-1}) vibration bands. DFT calculations of the Ni–Mo pair on N-doped graphene model predict a distance of 0.22 nm between the two metal atoms and suggest that the synergistic effect is derived from co-the adsorption of CO_2, preferentially on the Ni atom, and NO_3^- on the Mo atom, with the crucial C–N bond formation occurring between neighbor CO (on Ni) and NH (on Mo), thereby showing the synergistic effect arising from the presence of Ni and Mo at the catalytic site.

Broader context

Urea is one of the most important fertilizers, and it is also used as a co-monomer in the preparation of best-selling resins. Currently, urea is prepared by the reaction of ammonia and CO_2 through a process that requires heat obtained from burning fossil fuels. Fossil hydrocarbons with the generation of equivalent amounts of CO_2 are also required for the production of ammonia. In the present manuscript, the direct preparation of urea is described by the simultaneous electrochemical reduction of carbon dioxide and nitrate using renewable green electricity. The success of the process relies on a catalyst based on sites constituted of Ni–Mo atom pairs at a 0.24 nm distance, supported on a N-doped graphitic carbon, and based on the use of a pulsed electrolysis that shifts the voltage from −0.5 V (required for nitrate reduction) to −0.7 V (needed for carbon dioxide reduction) in seconds, allowing the simultaneous presence of intermediates from both carbon dioxide and nitrate on the surface of the electrocatalyst.

Introduction

Urea, one of the most important agricultural fertilizers, is also used as a monomer of synthetic polymers and resins and as a reagent in the synthesis of pharmaceuticals.[1,2] Its global annual production has reached about 100 million tons,[3] a number that is anticipated to rise further considering the increase in food demand of an expanding population. In spite of these high production volumes, current industrial urea synthesis methodologies are still based on over the one-hundred-year-old Haber–Bosch ammonia synthesis process and the Bosch–Meiser process,[4,5] with both reactions carried out at elevated temperatures and pressures. These conditions consume a significant amount of energy, resulting in substantial greenhouse gas emissions.[6] In the context of energy decarbonization and

[a] *Instituto Universitario de Tecnología Química (CSIC-UPV), Universitat Politècnica de València (UPV), Avda. De los Naranjos s/n, 46022, Valencia, Spain. E-mail: joalsan6@itq.upv.es, hgarcia@qim.upv.es*
[b] *Chemical and Biological Systems Simulation Lab, Centre of New Technologies, University of Warsaw, Warsaw, 02-097, Poland*

† Electronic supplementary information (ESI) available. See DOI: https://doi.org/10.1039/d5ey00056d

the implementation of renewable energy sources, the electrocatalytic co-reduction of CO_2 and nitrogen-containing wastewater has attracted considerable attention as a potential alternative to the current industrial synthesis.[7–9] This approach would not only lead to urea synthesis under much milder conditions, avoiding the consumption of fossil fuels to provide the required energy, but it would also represent a direct route to this chemical.

Electrocatalytic co-reduction of CO_2 and NO_3^-/NO_2^- for urea production was initially reported by Shibata *et al.*[10,11] This electrochemical urea synthesis comprises two concurrent cathodic processes, namely, CO_2 reduction (CO_2RR) and nitrate reduction (NO_3RR), that should ideally occur in a concerted manner with the adequate stoichiometry. Coupling of intermediates from the two processes at the cathode could produce urea. The prevailing consensus suggests that adsorbed CO (*CO) generated in CO_2RR and NH_x intermediates arising from the electrochemical hydrogenation of NO_3^- undergo C–N coupling at catalytic sites, resulting in urea formation, although the precise coupling precursors and mechanism remain elusive.[5,12] Conversion of CO_2 and NO_3^- into urea is a 16-electron process involving one highly stable reactant, with many intermediates and reaction steps, generally resulting in complex product distribution, low urea yield, and the inevitable competition of the hydrogen evolution reaction (HER).[13,14] It has been reported that bimetallic materials can exhibit higher electrocatalytic activity than monometallic catalysts, as a consequence of the better tuning of the solid surface sites through the electronic interaction of dissimilar metals, thereby adjusting the adsorption energy of reaction intermediates and the electron transfer to adsorbates, ultimately affecting electrocatalytic activity and product selectivity.[14–18]

Besides the nature of the electrocatalyst, the reported electrochemical urea synthesis is conducted using the traditional steady-state direct current mode in the vast majority of the cases, and product formation is controlled by mass transfer and diffusion layers.[19,20] In this context, prior studies have indicated that the migration of nitrate ions near the working electrode is limited by electrostatic repulsion, which makes nitrate diffusion difficult near the negative cathode surface, thereby negatively impacting on any mechanism leading to urea synthesis.[21] On the other hand, when coupling two different cathodic reactions as in the case of CO_2RR and NO_3RR, it could be that the optimal potential of one process is lower than that of the other. One possible way to overcome these hurdles could be to perform the electrocatalytic NO_3RR with a pulsed reduction potential that might result in a better control over the selectivity of desired products, and an enhanced urea efficiency.[22,23] Although pulsed electrocatalysis has not yet been used for urea synthesis, there have been several explorations in water splitting reactions and CO_2RR,[24–26] the latter being one of the required processes in urea synthesis.

The present study reports a novel Ni–Mo diatomic catalyst (NiMo-DASC) featuring dual active sites for urea electrosynthesis by coupling CO_2RR and NO_3RR. Specifically, it was considered that the Mo site could exhibit activity in NO_3RR based on the existing precedents,[27,28] whereas Ni would serve as active site for CO_2RR.[29,30] The rationale is that the combination of the two metals could show a synergism for urea synthesis. We used periodic pulse potential with peaks of more negative potentials to promote an enrichment of CO_2RR active intermediates on the cathode surface to be available for NH_x species and thereby improve urea faradaic efficiency (FE) and yield. Under the pulse potential protocol and optimal operational parameters, the urea FE and yield are among the best reported in literature,[31–33] with the NiMo-DASC catalyst reaching 31.8% and 11.3 mmol $g_{catalyst}^{-1}$ h^{-1}, respectively, exhibiting robust stability for 20 h electrolysis. Note that these data refer to the total catalyst mass and the values would be considerably higher if referred to the total mass of metals. *In situ* attenuated total reflectance surface-enhanced infrared absorption spectroscopy (ATR-SEIRAS) analysis corroborated that the pulse potential regime enriches the electrocatalyst surface with *CO intermediates, thereby facilitating urea generation. Density functional theory (DFT) calculations suggest that the process requires the simultaneous CO_2 and NO_3^- adsorption on Ni and Mo atoms, respectively, and that the key N–C coupling step occurs from adsorbed NH and CO in neighbor sites. This explains the synergism arising from sites constituted by two complementary atoms compared with single atom catalysis.

Material synthesis and characterization

NiMo-DASC catalyst was synthesized by pyrolyzing a mixture of $Ni(NO_3)_2$, $(NH_4)_6Mo_7O_{24}$, glucose, and melamine under an argon atmosphere (Fig. 1a). Ni-SAC and Mo-SAC were prepared following the same method, but using a single transition metal salt, either $Ni(NO_3)_2$ or $(NH_4)_6Mo_7O_{24}$. Details on the synthesis procedure are provided in the ESI.† The rationale in the selection of the precursors was to synthesize hetero diatomic site catalysts, and anionic molybdate ions having a high net negative charge should associate with dipositive nickel cations better than with ammonium ions, ensuring a pre-association between Ni and Mo before the thermal treatment. It was expected that the mutual attraction between anionic and cationic species would render dual atomic sites easier than employing precursors in which the transition metals have the same coulombic charge. This is confirmed by the lack of association using molybdenyl tris(acetylacetonate) (MoO_2acac_3, acac: acetylacetonate) as precursor. After the pyrolysis resulting in the formation of NiMo-DASC and before its use and characterization, all samples were grinded and then washed by 2 M HCl solution at 80 °C for 24 h under stirring to remove spurious loosely bound metal particles that are also formed in the process.

X-ray diffraction (XRD) patterns of the single atom catalysts (SAC) and dual atom single catalyst exhibit broad peaks at 11.5° and 25.3° corresponding to (001) and (002) diffractions of loosely stacked graphene oxide and graphitic carbon, respectively (Fig. S1, ESI†). No diffraction peaks related to metal compounds could be observed.

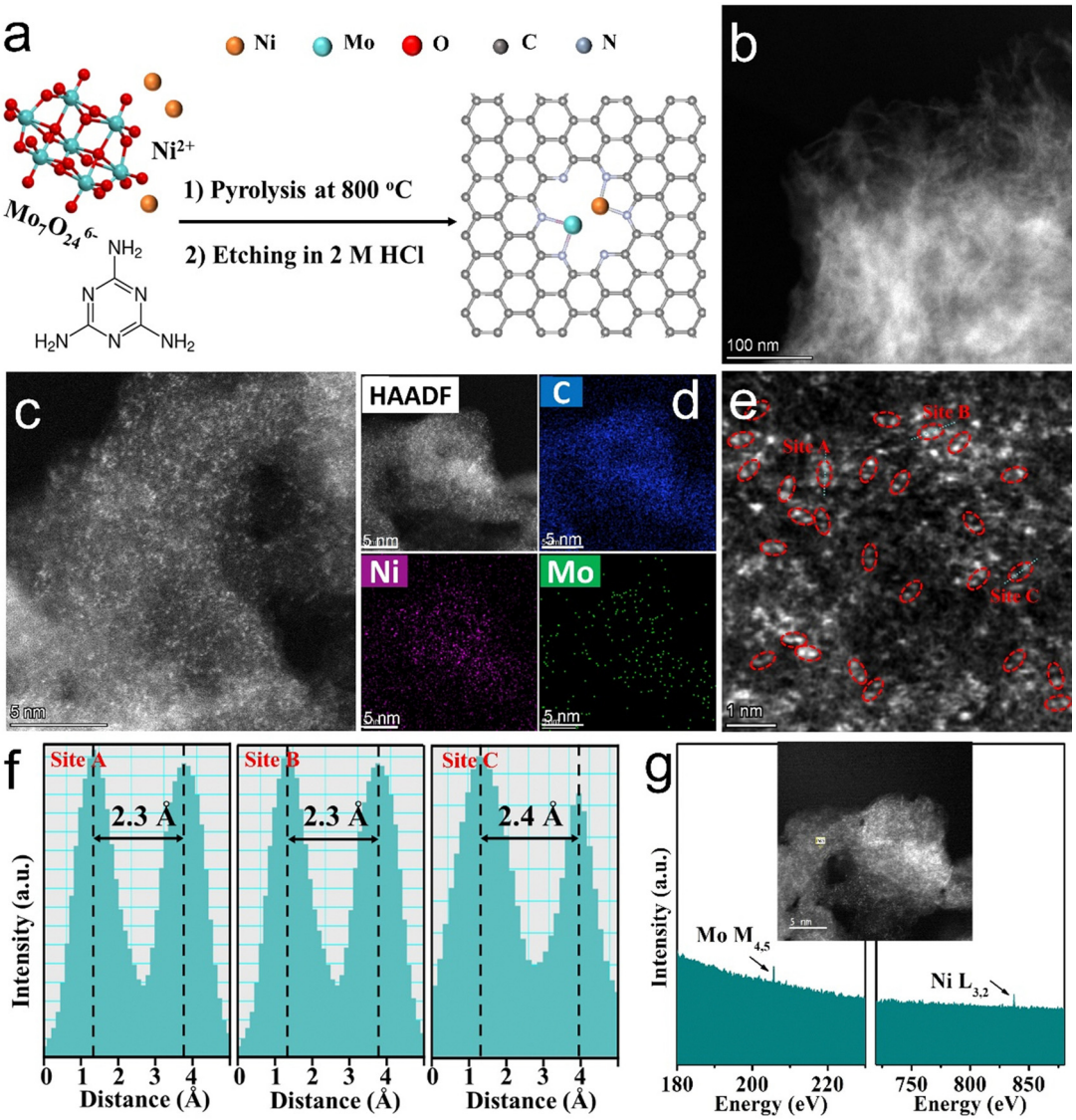

Fig. 1 (a) Schematic of catalyst preparation; (b) and (c) HAADF-STEM image of NiMo-DASC; (d) EDX elemental mapping images of Ni, Mo and C in NiMo-DASC; (e) HAADF-STEM image of NiMo-DASC in which diatomic NiMo sites separated by a distance of 2.3 Å are highlighted with red circles for clarity; (f) intensity profiles for three diatomic sites of image (e); (g) EELS spectrum of NiMo atomic sites indicated in the inset with a white line.

Dark field scanning electron microscopy (SEM) and scanning transmission microscopy (STEM) (Fig. S2 and Fig. 1b, ESI†) reveals that the materials present a porous morphology formed by two-dimensional sheets generated from glucose and melamine graphitization upon pyrolysis. Inductively coupled plasma-atomic emission spectroscopy (ICP-AES) of the samples after digestion with *aqua regia* indicates that the total metal loading in NiMo-DASC was 0.65 wt%, corresponding to 0.31 wt% of Ni and 0.34 wt% of Mo. As shown in Table S1 (ESI†), the total metal content of Ni-SAC and Mo-SAC was very similar, but constituted of a single metal, either Ni or Mo.

As collated in Table S1 (ESI†), NiMo-DASC shows slightly higher specific surface area (265.5 $m^2\ g^{-1}$) than Ni-SAC (226.2 $m^2\ g^{-1}$) and Mo-SAC (243.3 $m^2\ g^{-1}$). Raman spectra of all samples (Fig. S3, ESI†) exhibit the expected G and D bands at 1589 and 1374 cm^{-1}, characteristic of defective N-doped graphene (NG) formed in the carbonization of glucose and melamine mixture, while no obvious vibration bands for Ni or Mo oxides or carbides were observed in the low-frequency region, in good agreement with the XRD results.

The dark-field STEM and energy-dispersive X-ray spectroscopy (EDS) elemental mapping of NiMo-DASC (Fig. 1c, d and Fig. S4, ESI†) indicate the uniform distribution of Ni and Mo on the entire NG. The atomic distribution of NiMo-DASC was further analyzed by aberration-corrected high-angle annular dark-field scanning transmission electron microscopy (AC-HAADF-STEM) with atomic resolution. Fig. 1e shows an illustrative image of NiMo-DASC in which a considerable number of atom-sized twin bright dots are uniformly dispersed on the NG support. These atom pairs have been highlighted in the image with red circles for a better visualization. The distance between the two atoms was measured and found to be

consistent ~0.24 nm (Fig. 1f), implying the formation of atomic pairs *via* metal–metal (Ni–Mo) bonds. Electron energy loss spectroscopy (EELS) further revealed that the bright dots were due to the coexistence of pairs of Ni and Mo atoms (Fig. 1g).

The elements present in the three electrocatalysts under study, the oxidation state of the surface atoms and their coordination sphere were analyzed by X-ray photoelectron spectroscopy (XPS). In the high-resolution XPS core levels of NiMo-DASC, the Ni signal was positively shifted about 0.3 eV compared with NiSAC (Fig. 2a), and the Mo peak was negatively shifted compared with that of Mo-SAC, also by about 0.3 eV (Fig. 2b), indicating that the charge transfer from Mo to Ni in the dual atom sites are present in NiMo-DASC.[34,35] The N 1s core level of the three catalysts show the existence of pyridinic (~398.1 eV), metal–N (~399.2 eV), pyrrolic (~400.6 eV), quaternary (~401.6 eV) and oxidized (~402.9 eV) N species (Fig. S5, ESI†).[36] The percentage of metal–N species in the total N atom was 11.8%, 12.2% and 19.8% for Ni-SAC, Mo-SAC, and NiMo-DASC, respectively. The presence of this N component suggests that the transition metal atoms are anchored on the defective NG sheets *via* metal–N coordination, as reported in other cases.[12,13,37,38]

Fig. 2c–f shows the X-ray absorption near-edge spectra (XANES) and extended X-ray absorption fine structure (EXAFS) of the three electrocatalysts. The Ni K-edge XANES of NiMo-DASC (Fig. 2c) confirms that Ni has an oxidation state between Ni(0) and NiO (+2). Similarly, the Mo K-edge XANES of NiMo-DASC (Fig. 2d) resides between Mo(0) foil and MoO_3 (+6), indicating that the oxidized state of Mo in NiMo-DASC is about +III and +IV. Compared with Ni-SAC, a minor shift of the Ni K-edge in NiMo-DASC toward high energy implies a slight increase in the oxidation state of Ni owing to a lower electron density. Mo atoms in NiMo-DASC were slightly reduced due to the electron density transfer of Ni with respect to Mo-SAC. Such a trend obtained by the X-ray absorption spectra agrees perfectly with the XPS analyses and is in accordance with the relative electronegativity of the two elements, with Ni (1.91) being less electronegative than Mo (2.16). Therefore, Mo attracts electrons from Ni.

EXAFS fitting data for the three samples are summarized in Table S2 (ESI†). The k^3-weighted Fourier transform (FT) from the Ni K-edge EXAFS spectra (Fig. 2e) shows that the major peaks of NiMo-DASC and Ni-SAC are located at ~1.35 Å, which corresponds to the first shell scattering of the Ni–C/N

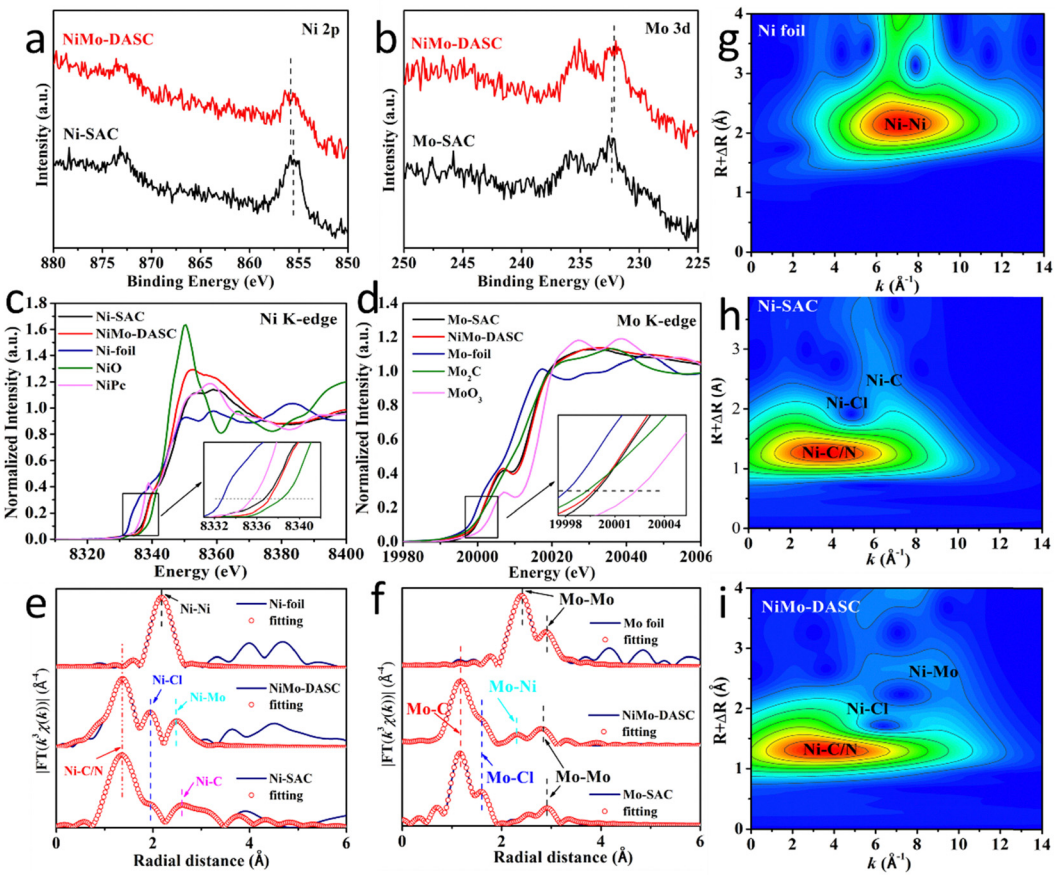

Fig. 2 High-resolution XPS peaks of (a) Ni 2p and (b) Mo 3d of the three samples; (c) Ni K-edge XANES spectra of Ni-SAC, NiMo-DASC, Ni foil, NiO and NiPc (Pc: phthalocyanine); (d) Mo K-edge XANES spectra of Mo-SAC, NiMo-DASC, Mo foil, Mo_2C and MoO_3; (e) k^3-weighted FT of $\chi(k)$-function from the Ni K-edge EXAFS; (f) k^3-weighted FT of $\chi(k)$-function from the Mo K-edge EXAFS; wavelet transform images of the Ni K-edge from (g) Ni foil, (h) Ni-SAC and (i) NiMo-DASC.

coordination. The second peak at 1.93 Å is attributed to Ni–Cl coordination due to the washing process of chlorine-containing acids to remove excess metal during material preparation. However, it is unlikely that this residual Cl would remain under the conditions of the electrocatalytic urea formation, considering the high concentration of CO_2 and NO_3^- in the electrolyte that would replace any residual Cl from the Ni coordination. Notably, the third peak at 2.45 Å for NiMo-DASC is comparable with the first shell distance of Ni foil (2.21 Å), suggesting the presence of a metal–metal diatomic configuration.[14,36] This distance agrees with the distance of 2.4 Å measured for the dual Ni–Mo pairs by HAADF-STEM (Fig. 1f).

Similarly, the major peaks at ~1.17 Å for NiMo-DASC and Mo-SAC in Fig. 2f are ascribed to Mo–C coordination. The peak at 2.31 Å for NiMo-DASC further confirms the presence of a metal–metal diatomic configuration. A slight Mo-Mo signal is detected in NiMo-DASC and Mo-SAC, indicating that the samples have a small amount of Mo particles. The k^3-weighted FT spectra indicate that the metal–metal distance in NiMo-DASC is longer than Ni–Ni coordination in Ni foil and shorter than Mo–Mo coordination in Mo foil, verifying the existence of heterogeneous Ni–Mo sites in NiMo-DASC. On the other hand, the first shell scattering (Ni–C/N and Mo–C) for NiMo-DASC displays asymmetry and slightly decreased magnitude compared with Ni-SAC and Mo-SAC, indicating that the chemical state of Ni is altered by the coupling Mo atom. As shown in Fig. 2g–i, wavelet transform (WT)-EXAFS allowed us to conclusively identify the existence and intensity of the metal–N and metal–metal bonds in NiMo-DASC. Therefore, both, HAADF-STEM and XAS conclusively prove the dual NiMo atom configuration in the NiMo-DASC sample and the single atom nature of Ni-SAC and MO-SAC.

Electrocatalytic urea synthesis

The intrinsic NO_3RR performance of catalysts was initially investigated using a H-cell system using a 0.05 M KNO_3 aqueous solution as electrolyte. First, constant potential NO_3^- electrolysis was performed in the range between −0.3 and −0.7 V *versus* RHE. The FE toward NH_3 and NO_2^- was measured at different potentials by colorimetric quantification of these two products with UV-Vis spectrophotometry employing the Nessler and Griess reagent for NH_3 and NO_2^-, respectively. Fig. 3a shows that NiMo-DASC exhibits prominent NH_3 FE values and higher yield rates. At the optimum potential of −0.5 V *vs.* RHE, the FE of NH_3 for NiMo-DASC reaches 86.3% with a yield rate of 49.32 $mmol_{NH_3}\ g_{catalyst}^{-1}\ h^{-1}$. The FE of H_2 increases slightly as the potential increased. Besides, there is zero content of N_2H_4 in the liquid product. In comparison, the NO_3RR performance of Ni-SAC and Mo-SAC are shown in Fig. S6 (ESI†), with the latter showing more than twice the NH_3 yield rate than Ni-SAC at all investigated potentials. This comparison indicates that Mo sites have higher activity than Ni sites for electrocatalytic NO_3RR, although they are accompanied by higher FE of H_2. This is in agreement with previous

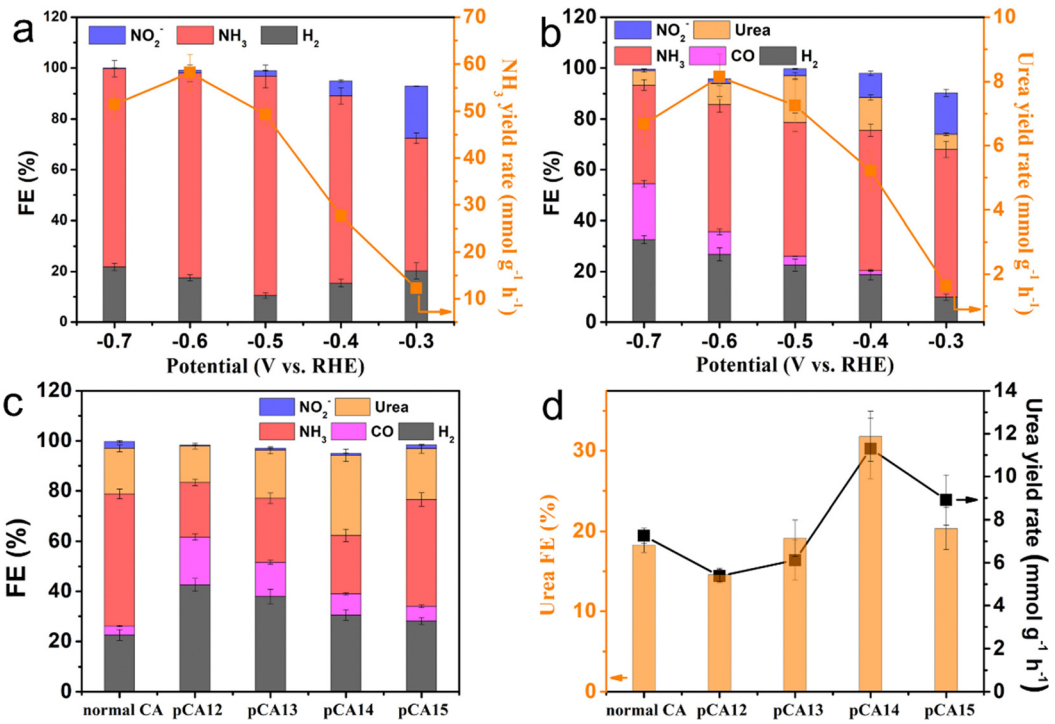

Fig. 3 Evaluation of the electrocatalytic performance of NiMo-DASC catalyst. (a) FE and NH_3 yield rate of NiMo-DASC for NO_3RR; (b) CO_2 and NO_3^- co-electroreduction performance with constant chronoamperometry (CA); (c) and (d) urea electrosynthesis performance with pulsed CA (pCA). Different pulsed chronoamperometry conditions are denoted as pCA*xy*, where *x* represents the electrolysis time at −0.7 V *vs.* RHE and *y* represents the electrolysis time at −0.5 V *vs.* RHE.

reports in the literature about the relative efficiency for NO_3RR of Mo and Ni materials.[39] In addition, the NH_3 yield of all three samples only slightly increases with increasing potential to −0.7 V, which could be attributed to the mass transfer limitation.

To further upgrade the scope of the products, CO_2 was also introduced into the electrocatalytic system with the aim to couple CO_2RR and NO_3RR. The electrochemical performance evaluation of single or dual atom catalysts was carried out under ambient conditions using the chronoamperometry method in a CO_2-saturated 0.1 M $KHCO_3$ + 0.05 M KNO_3 electrolyte. In these electrocatalytic reactions, gaseous products were quantified by gas chromatography (GC) and liquid products were quantified by colorimetry with UV-Vis spectrophotometry (Fig. S15–S18, ESI†). As shown in Fig. 3b, an outstanding urea yield rate of 7.26 $mmol_{urea}\ g_{catalyst}^{-1}\ h^{-1}$ can be achieved at the potential of −0.5 V *vs.* RHE. A volcano curve was also seen for FE, and, impressively, the highest FE toward target urea to 18.3% was obtained under the same potential. The CO FE is lower than that without NO_3^- at various potentials (Fig. S7, ESI†), which is probably ascribed to the consumption of CO for urea formation and competition in parallel with NO_3RR. Meanwhile, NH_3 FE and yield also shows the same trend, which strongly suggest that there is a competitive relationship between urea and CO/NH_3 synthesis, and that the coupling of C and N-containing intermediates inhibits the formation of CO and NH_3 as the final products.[40] In addition, NiMo-DASC exhibits more than twice the urea yield compared with Ni-SAC sample (Fig. S8, ESI†), which is probably attributed to the higher NO_3RR intermediate population density produced on the Mo sites. Mo-SAC has already exhibited higher NH_3 evolution activity than Ni-SAC during NO_3RR (Fig. S6, ESI†). Surprisingly, Mo-SAC only shows a very low urea FE and yield rate, which is ascribed to its low activity for CO_2RR (Fig. S7b, ESI†). The ingenious design of NiMo-DASC as dual active sites with Ni and Mo serving as active sites for CO_2RR and NO_3RR, respectively, results in an unexpectedly excellent performance. Firm confirmation of the source of the derived urea from CO_2 and NO_3^- was obtained through isotope labeling experiments (Fig. S9, ESI†). Thus, the same chronoamperometry measurement was performed using $^{13}CO_2$ and $^{15}NO_3^-$ as carbon and nitrogen precursor, respectively, and NMR isotope labeling experiments further verified that C,N-urea originated from the coupling of nitrate reduction and CO_2. To gain information on the possible mechanism of urea synthesis, the same experiment was performed using NH_4^+ instead of NO_3^- and CO (or HCOOH) instead of CO_2. There was no urea generated from these precursors (Fig. S10, ESI†). This shows that carbon–nitrogen coupling occurs before NO_3^- or CO_2 are completely reduced to the final product.

Pulsed electrolytic urea synthesis

Although the ingenious dual-active site catalyst design demonstrates better urea production performance compared with single-atom catalysts, the low urea FE is still the main obstacle restricting its application. Considering that the NH_3 yield rate on NiMo-DASC is more than four times higher than that of CO (Fig. 3a and Fig. S7a, ESI†), it appears a logical conclusion that CO_2RR is the process limiting its co-reduction with NO_3RR to form urea. To overcome this hurdle and to enhance CO_2RR relative to NO_3RR, a pulse electrosynthesis strategy was explored. It was observed that these pulsed experiments greatly improved the FE and yield of electrosynthesized urea, probably due to the higher CO_2RR efficiency under pulsed conditions and accumulation of adsorbed *CO active intermediates. Specifically, unlike conventional chronoamperometric electrolysis, the CO_2 mass transfer and concentration of the *CO intermediate on the catalyst surface is increased by applying a short high pulse voltage (−0.7 V *vs.* RHE), which almost does not affect the NH_3 yield (Fig. 3a and Fig. S6, ESI†), thereby synthesizing urea at −0.5 V.

The applied voltage for the pulsed experiments is shown in Fig. S11 (ESI†). Fig. 3c and d compares the electrochemical urea synthesis performance of constant chronoamperometry (CA) and pulsed electrolysis with different pulsed periods. Compared with constant-potential electrolysis, the selectivity of each product changes significantly under pulsed conditions, and the FE of CO increases dramatically. The electrolysis time at −0.5 V ($t_{0.5}$) under pulse conditions has a significant impact on product selectivity. When $t_{0.5}$ = 4 s, both FE and yield of urea increased significantly, reaching urea FE of 31.8% and a yield of 11.3 mmol $g_{catalyst}^{-1}\ h^{-1}$, which is 1.7 times that of constant-potential electrolysis. Furthermore, if urea yield is given by mass of metal rather than the total catalyst mass, a value of 1738 mmol $g_{Ni+Mo}^{-1}\ h^{-1}$ is calculated. The pulse time at −0.7 V ($t_{0.7}$) was also studied (Fig. S12, ESI†), and the results showed that an excessively long pulse time can only produce the mixing effect of −0.5 V and −0.7 V chronoamperometry. A pulse period that is too short results in a reduction in reactivity, which can be attributed to the adverse effects of the capacitive current period and insufficient time for ions to selectively adsorb on the electrode surface.[23] In addition, as shown in Fig. S13 (ESI†), the FE of urea was always maintained above 30% in the 20 h pulsed experiment, demonstrating the potential application of pulsed electrolysis in this reaction.

In situ IR measurements

In situ electrochemical Raman spectroscopy studies were carried out for the NiMo-DASC sample at open circuit potential (V_{oc}) and at a cathodic potential range of −0.35 to −0.65 V. The peak located at 1553 cm^{-1} was observed in Fig. S14a (ESI†). This vibration band can be assigned to adsorbed carboxylate $*CO_2^-$ associated with CO_2RR.[41,42] The 1553 cm^{-1} peak intensity gradually strengthens with potential. Additional peaks at 1049 and 1350 cm^{-1} have been previously attributed to NO_3^- and carbon paper signal, respectively.[43] *In situ* ATR-SEIRAS was employed to monitor the NiMo-DASC interface to follow the evolution of electrochemical reaction intermediates. As shown in Fig. S14b (ESI†), ATR-SEIRAS was first applied at −0.3 to −0.7 V *vs.* RHE. The signals at 1937 and 1404 cm^{-1} are attributed to the stretching mode of *CO associated with CO_2RR and the adsorption of CO_2 molecules. The infrared

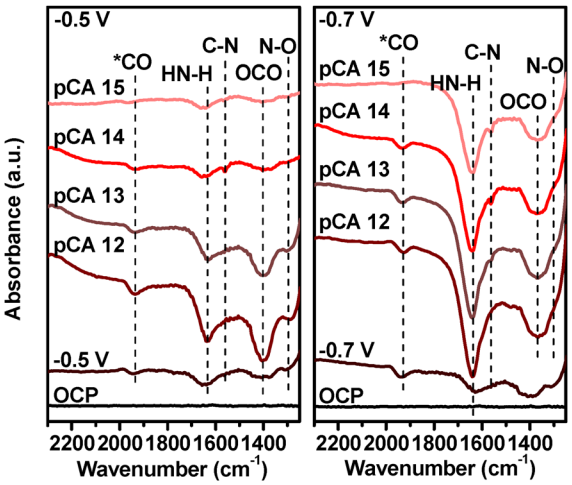

Fig. 4 *In situ* ATR-SEIRAS spectra recorded for NiMo-DASC at two different potentials under pulsed conditions.

bands at 1636 and 1296 cm^{-1} correspond to the H–N–H bending vibration of $*NH_2$ and the N=O stretching vibration of $*NO_2$ of NO_3RR, respectively.[43] The slight absorption signal at 1567 cm^{-1} can be attributed to the stretching mode of C=N during the evolution of urea.[44] The signal evolution of related intermediates was further studied under pulsed electrolysis conditions. Fig. 4 shows the extracted infrared signals collected under −0.5 and −0.7 V *vs.* RHE respectively. A stronger *CO intermediate and adsorbed CO_2 signal was demonstrated at the pulse potential of −0.7 V compared with −0.5 V. Obviously, the pulse potential of −0.7 V significantly increases the active *CO concentration at the catalyst interface, which is conducive to further C–N coupling to produce urea. The signal shift of *CO should be due to the change of chemical environment from carbon species to NH_x species on the way to urea formation. The significant enhancement of the C–N signal under pulsed conditions is also in good agreement with the results of electrochemical performance experiments.

DFT calculations on the reaction mechanism

DFT simulations were performed to elucidate the urea formation mechanism. The chosen model system for the catalytic surface consists of a dual Ni–Mo atom site anchored to a doped graphene sheet through six nitrogen coordination, as indicated by experimental characterization (see Fig. S19, ESI†). The distance between the two metal centres has been computed to be 0.22 nm, which is in very good agreement with the experimental aberration corrected STEM analysis value of 0.23 nm (Fig. 1f).

According to the experimental analyses commented above, in the models, CO_2 was adsorbed on Ni, while NO_3^- was adsorbed on Mo. As mentioned above, the conversion of nitrate to urea is a complex process involving 16 electrons, corresponding to 16 steps, two of which are the critical C–N bond couplings. Thus, assuming that the two C–N bond formation steps are the rate determining elementary processes, it is necessary to consider which pathways would lead to more favourable coupling steps. Since there is no available information on the adsorption of the different gaseous species on the DASC, we considered different scenarios in which (i) NO_3^- is first adsorbed to form $*NO_3$ and then CO_2 is added to form a $*NO_3$–$*CO_2$ pair (where the '–' indicates the adsorption on different metal centres), (ii) CO_2 is first adsorbed to form $*CO_2$ and then NO_3^- is added to obtain the $*NO_3$–$*CO_2$ pair, and (iii) both NO_3^- and CO_2 are added simultaneously to the substrate. This can be very important, as the reaction mechanism can change depending on the adsorption sequence, either favoring CO_2RR or ammonia reduction instead of urea formation. We recall here that Sabatier's principle states that a too strong or a too weak adsorption is not beneficial to the coupling process, as the first case deactivates the catalytic activity of the adsorbate, while the second one can lead to desorption of the adsorbate. Generally, a good adsorption energy should have a small, negative value close to zero, favoring the interaction between the adsorbate and the substrate, but not strong enough to inhibit the reaction. In the current case, we have a two two-step adsorption (NO_3^- followed by CO_2, or the opposite) and a one-step adsorption process that can compete. The simultaneous adsorption of both gaseous molecules leads to a strong, negative adsorption energy of −1.86 eV, which is too strong and impedes the reaction to proceed further. If NO_3^- is adsorbed first, we obtain an adsorption energy of −1.83 eV, and the subsequent adsorption of CO_2 for a strong destabilization of the obtained $*NO_3$–$*CO_2$ system, with a positive energy of 0.38 eV suggesting that this pathway is not thermodynamically stable. The reverse process, with an initial adsorption of CO_2 leads to an energy stabilization of −1.02 eV, and the subsequent adsorption of NO_3^- to an overall −0.43 eV stability of the $*NO_3$–$*CO_2$ system, suggesting that this is the favourable sequence.

The obtained differences are not only related to the energetics, but also to the conformation of the adsorbates, as depicted in Fig. 5. The observed differences in adsorption geometries and energies are reflected in the different electronic properties of the adsorbates, such as the partial density of states (PDOS) and the charge density difference (Fig. 5). The PDOS of the surface shows that the d orbitals of both Ni and Mo catalytic centres are very close to the Fermi energy, suggesting the high activity of this DASC and a partial charge transfer of 0.33 and 1.12 $|e^-|$. The adsorption of NO_3^- leads to the formation of two chemical bonds between the oxygen atoms and the Mo centre, with distance of 0.21 nm. The PDOS analysis shows that the d orbital states of Ni are now further away (*i.e.*, lower in energy) from the Fermi energy, with the Mo atom protruding from the catalyst plane, since it is now activated. This is confirmed by the amount of charge transferred to NO_3^-, with value of −0.78 $|e^-|$ and the significant increase in positive charge over Mo of 1.49 $|e^-|$, and to a less extent on Ni, with a value of 0.42 $|e^-|$. A different scenario arises when the CO_2 adsorption is considered, with the molecule bent and interacting with both metal centres, with a Mo–O bond

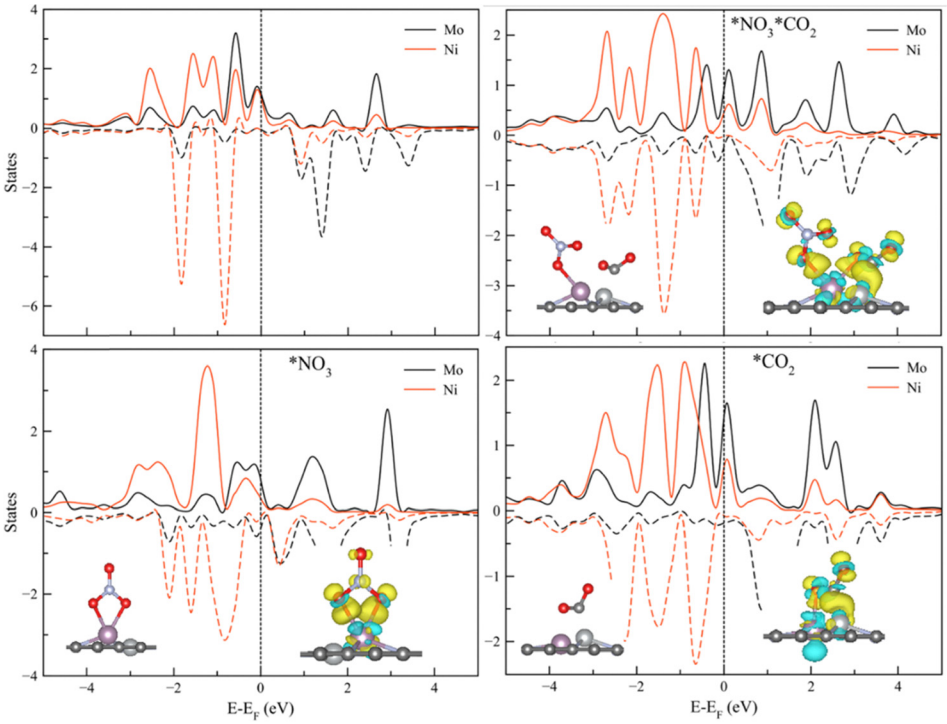

Fig. 5 Projected density of state (PDOS) analysis of the spin polarized d orbitals for the bare surface and the adsorption of the NO_3^- and CO_2 gases (spin up in solid line, spin down with dotted line). The inset shows the charge density difference for the adsorption of NO_3^-, CO_2 and when adsorbed at the same time. The yellow (blue) color represents loss (accumulation) of electrons. The black dotted lines represent the Fermi energy level.

distance of 0.20 nm and Ni–C of 0.19 nm, and the Ni atom being out of the plane of the catalytic surface, indicating the activation of this metal centre due to a rearrangement of the d orbitals. In fact, the PDOS analysis shows that both Ni and Mo d states are now closer to the Fermi energy, implying that both metals are activated. The charge density difference and charge transfer (CT) analyses confirm this view, as the CT to CO_2 has a value of -1.01 $|e^-|$, while on Ni, it is the same as for the NO_3^- adsorption (0.42 $|e^-|$), and for Mo it increases up to 1.69 $|e^-|$. Finally, for the case when both NO_3^- and CO_2 are adsorbed together, a Mo–O bond distance of 0.21 nm for NO_3^- and Ni–C of 0.19 nm for CO_2 are obtained, which are shorter than when the two molecules are considered isolated, due to a stronger adsorption energy. These geometries and energy values are the result of a different hybridization of the metal centres, which are now both active and protruding out of the graphene plane. The PDOS analysis confirms this hypothesis, as now the d orbitals states of both Ni and Mo are closer to the Fermi energy. Moreover, the charge density difference and CT analyses quantify this effect, with an excess of electron over the adsorbed molecules with a value of -0.84 $|e^-|$ for CO_2 and -0.76 $|e^-|$ for NO_3^-, while the positive charge on the catalytic centres has a value of 1.66 $|e^-|$ for Mo and 0.46 $|e^-|$ for Ni, in an intermediate range of value compared with the isolated adsorptions. Therefore, the above analysis confirms that the preferred pathway is the adsorption of CO_2 followed by NO_3^-. The possible presence of HCl (as a residual of the synthetic process) has been considered and the analysis reported in the ESI.†

As experimental observations indicate that an applied bias of -0.5 V drives the reaction towards the formation of ammonia, we consider the reduction of NO_3^- up to the formation of NH at this potential as a likely pathway in the DFT modelling. This pathway is referred to as the Langmuir–Hinshelwood mechanism that proceeds by coupling adsorbed CO* and NH* species to form NHCO*. As reported by Santoro,[45] the C-intermediate *CO could couple with different N-intermediates such as *NO, *NH, *NH_2 or *H_2NOH. Hence, for the C–N coupling reactions of *CO and *NH or *NH_2, these two species act as a base and attack the positively charged center of CO*, promoting the formation a C–N bond and consequently the formation of urea instead of ammonia. Once the NH intermediate is formed, we compute an increase in the potential at -0.7 V (to simulate the pulsing potential technique) to allow for the reduction of CO_2 to CO, and then return to -0.5 V to obtain urea. The full reaction pathway with applied potentials of -0.5 and -0.7 V is reported in Fig. S20 (ESI†).

Hence, the reaction starts with the adsorption of *NO_3–*CO_2, which is thermodynamically favourable, with a calculated adsorption energy of -0.93 eV. The first protonation forms *NO_3H–*CO_2, which is less stable than the precursors by 0.33 eV at an applied potential of -0.5 V. Water elimination leads to the formation of *NO_2–*CO_2, which is strongly stabilized, lying at -3.17 eV. Protonation of this intermediate leads to *NO_2H–*CO_2 formation, which is less stable than the precursor by 0.36 eV. The second water elimination leads to the formation of *NO–*CO_2, which is strongly stabilized compared

with its precursor by −3.37 eV. The subsequent protonation leas to *NOH–*CO_2, which is the potential-dependent step (PDS) of the whole reaction, for which the maximum reaction free energy is 0.63 eV at −0.5 V *vs.* standard hydrogen electrode (SHE). The obtained PDS is comparable with the 0.62 eV reported in the literature for the formation of urea on a FeNi dual atom catalysts for the same intermediate formation.[46] This step is also the PDS when no bias is applied, with a limiting potential U_L value of −1.13 eV ($U_L = -\Delta G_{PDS}/e$), meaning that this potential is required to have a barrierless reaction pathway. From this intermediate on, all the subsequent paths are thermodynamically more stable than their precursors, and the reaction proceeds spontaneously (Fig. 6a). *NOH–*CO_2 will further exothermically dissociate into *NHOH–*CO_2 and *NH–*CO_2 by accepting two protons from the solvent and eliminating a water molecule.

From this intermediate, we increase the potential up to −0.7 V to favour the CO_2 reduction to CO and further allow for the C–N coupling to eventually obtain urea. The protonation of the oxygen atom leads to the formation of *NH–CO_2H, and the following protonation and water elimination lead to the formation of *NH–CO, which is more stable than the previous intermediate by −0.39 eV. We consider this intermediate as the key step for the formation of urea, as it has been reported that these two species are critical precursor for the C–N bond coupling leading to the product.[45] The second NO molecule would then be attached to the newly generated Ni site (Fig. S21, ESI†). The next step is the first crucial C–N coupling between *NH and the adjacent *CO to obtain *NHCO in a thermodynamic spontaneous process, with the coupled intermediate being more stable than the precursor by −0.62 eV. The activation energy obtained from the transition state (TS) of this reaction step is 0.61 eV, which has a lower value than the PDS (1.13 eV), confirming that the reaction proceeds with a late TS spontaneously towards urea formation (Fig. S22, ESI†). Moreover, the Ni centre becomes free with the formation of *NHCO, allowing for the absorption of a NO molecule. Thus, the *NHCO on Mo and *NO on Ni can steadily couple together and are converted into *NHCONO, which is the second crucial intermediate with an energy stabilization of −0.79 eV. Protonation of the oxygen leads to the formation of *NHCONOH, and subsequent water removal forms *NHCON, which is highly stabilized compared with the previous intermediate by −2.21 eV. From this intermediate, additional protonation steps of the two nitrogen atoms eventually lead to the formation of urea.

Since there is a possible competition pathway from *NH–*CO to form *NH_2–*CO either leading to urea or ammonia reduction, we present both of them here (Fig. 6b). The competing pathway from *NH–*CO proceeds with the proton addition leading to *NH_2–*CO, which is exothermic with an energy stabilization of −0.90 eV, and it is more stable than the C–N coupling by 0.29 eV. From this intermediate, either the C–N coupling to obtain *NH_2CO or the proton addition leading to *NH_3–*CO are possible. While the first path is endothermic, requiring an additional 1.09 eV of energy input, the second path leads to the exothermic ammonia formation, with a small stabilization energy of −0.10 eV. Considering the reaction when the external bias in not considered ($U = 0$), we observe that an energy of 1.59 eV is required for the *NH_2CO coupling step. Hence, this pathway is not favoured form a thermodynamical point of view. On the other hand, as observed experimentally, ammonia can be formed as only 0.4 eV are needed to obtain it, and when we applied the pulsed bias, it is large enough to allow for its formation. Yet, the *NH_3–*CO intermediate is less stabilized than the *NHCONO one by 0.4 eV, which explains the high urea formation despite the concomitant ammonia production.

Finally, we considered the hydrogen evolution reaction (HER) over the two catalytic centres. The HER is unfavourable on both metals, with absorption free energies of −0.51 and −0.72 eV on Ni and Mo, respectively, compared with the adsorption of NO_3 and CO_2.

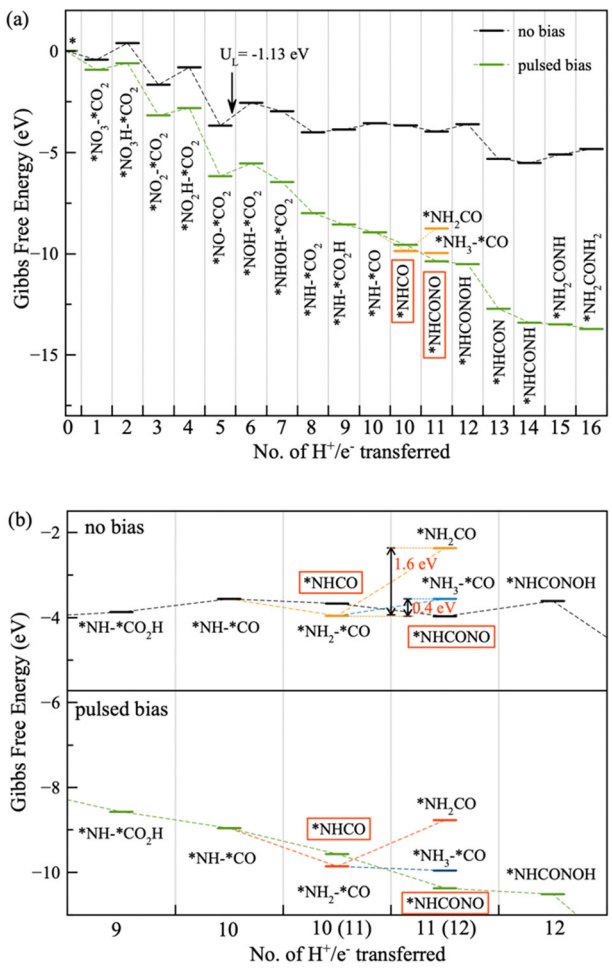

Fig. 6 (a) Gibbs free energy reaction pathway for the urea formation. The hyphen indicates the adsorption of both species on different metals. The two C–N coupling steps are highlighted. (b) Competitive ammonia reduction path.

Conclusions

The present study shows the synergistic effects that arise when two complementary metal atoms are combined in single sites.

Thus, by wise selection of negative ($Mo_7O_{24}^{6-}$) and positive (Ni^{2+}) precursors, sites of Ni–Mo pairs (0.23 nm distance) have been installed on N-doped graphitic carbon residues. These dual Ni Mo sites are efficient electrocatalysts for urea synthesis, with the efficiency derived from the complementary roles of Ni and Mo preferentially effecting CO_2 reduction and NO_3^- reduction, respectively, as deduced from the comparison with Ni-SAC and Mo-SAC materials. By applying a pulsed protocol in which the electrolysis is carried out at −0.5 V *vs.* RHE with short pulses of −0.7 V *vs.* RHE, NiMo-DASC reaches a 31.8% faradaic efficiency towards urea and a urea yield of 11.3 mmol $g_{catalyst}^{-1}$ h^{-1} (1738 mmol g_{Ni+Mo}^{-1} h^{-1}), while exhibiting robust stability for 20 h electrolysis. *In situ* IR spectra show the presence on the catalyst surface of adsorbed CO and NH_x species which evolve to urea. DFT calculations indicate that first adsorption of CO_2 (on Ni atom) followed by NO_3 (on neighbor Mo) is the most likely starting point of urea formation, with the crucial C–N bond formation taking place, between adsorbed CO and NH species. Thus, the present results show the synergism that arises from the combination of two metals with different roles on the catalytic site due to the preference of one metal atom for binding and reducing CO_2 (Ni) and the other metal to reduce NO_3 (Mo) and the advantage of potential pulse to activate different processes.

Data availability

Data are available from the corresponding authors upon reasonable request.

Conflicts of interest

There are no conflicts to declare.

Acknowledgements

Financial support from the Spanish Ministry of Science and Innovation (CEX-2021-001230-S and PDI2021-0126071-OB-CO21, funded by MCIN/AEI/10.13039/501100011033) and Generalitat Valenciana (Prometeo 2021/038 and Advanced Materials programme Graphica MFA/2022/023, with funding from European Union NextGenerationEU PRTR-C17.I1) are gratefully acknowledged. Participation in the EU project SUPERVAL is grateful acknowledged. J. A. thanks the Spanish Ministry of Science and Innovation for a Ramon y Cajal research associate contract (RYC2021–031006-I financed support by MCIN/AEI/10.13039/501100011033 and by European Union/NextGenerationEU/PRTR), and Generalitat Valenciana (CIGE 2022-093) financed by European Union-Next Generation EU, through the Conselleria de Innovación, Universidades, Ciencia y Sociedad Digital. J. H. thanks the Chinese Scholarship Council for the doctoral fellowship. S. O. thanks the National Science Centre, Poland (grant no. UMO-2023/50/E/ST4/00197) and the ''Excellence Initiative – Research University'' (IDUB) Program, Action I.3.3–''Establishment of the Institute for Advanced Studies (IAS)'' for funding (grant no. UW/IDUB/2020/25). The computation was carried out with the support of the Interdisciplinary Center for Mathematical and Computational Modeling at the University of Warsaw (ICM UW) under grants no. G83-28 and GB80-24. We acknowledge the Polish high-performance computing infrastructure PLGrid for awarding this project access to the LUMI supercomputer, owned by the EuroHPC Joint Undertaking, hosted by CSC (Finland) and the LUMI consortium through PLL/2023/05/016760.

References

1 R. Prasad, Fertilizer urea, food security, health and the environment, *Curr. Sci.*, 1998, **75**, 677–683.
2 E. S. Wibowo, B.-D. Park and V. Causin, Recent advances in urea–formaldehyde resins: converting crystalline thermosetting polymers back to amorphous ones, *Polym. Rev.*, 2022, **62**, 722–756.
3 J. Qiao, Y. Liu, F. Hong and J. Zhang, A review of catalysts for the electroreduction of carbon dioxide to produce low-carbon fuels, *Chem. Soc. Rev.*, 2014, **43**, 631–675.
4 J. Meessen, Urea synthesis, *Chem. Ing. Tech.*, 2014, **86**, 2180–2189.
5 M. Muhyuddin, Z. Giovanni, P. Mustarelli, J. Filippi, A. Lavacchi, L. Elbaz, Y.-H. Chen, P. Atanassov and C. Santoro, Urea Electrochemical Production Using Carbon Dioxide and Nitrate: State of the Art and Perspectives, *Energy Environ. Sci.*, 2024, **17**, 3739–3752.
6 A. Khan, A. Abbas and R. Dickson, Towards a low-carbon future: exploring green urea synthesis for sustainable agriculture, *Green Chem.*, 2024, **26**, 1551–1565.
7 C. Mao, J. Byun, H. W. MacLeod, C. T. Maravelias and G. A. Ozin, Green urea production for sustainable agriculture, *Joule*, 2024, **8**(5), 1224–1238.
8 Y. Wang, D. Chen, C. Chen and S. Wang, Electrocatalytic Urea Synthesis via C–N Coupling from CO_2 and Nitrogenous Species, *Acc. Chem. Res.*, 2023, **57**, 247–256.
9 Q. Zhao, Y. Zhang, D. Cao and M. Shao, The Prospects of Urea Manufacturing via Electrochemical Co-reduction of CO_2 and Nitrates, *Curr. Opin. Electrochem.*, 2024, **45**, 101479.
10 M. Shibata, K. Yoshida and N. Furuya, Electrochemical synthesis of urea at gas-diffusion electrodes: Part II. Simultaneous reduction of carbon dioxide and nitrite ions at Cu, Ag and Au catalysts, *J. Electroanal. Chem.*, 1998, **442**, 67–72.
11 M. Shibata, K. Yoshida and N. Furuya, Electrochemical synthesis of urea at gas-diffusion electrodes: III. Simultaneous reduction of carbon dioxide and nitrite ions with various metal catalysts, *J. Electrochem. Soc.*, 1998, **145**, 595.
12 J. Liu, X. Guo, T. Frauenheim, Y. Gu and L. Kou, Urea Electrosynthesis Accelerated by Theoretical Simulations, *Adv. Funct. Mater.*, 2023, **34**(14), 2313420.
13 M. Jiang, M. Zhu, M. Wang, Y. He, X. Luo, C. Wu, L. Zhang and Z. Jin, Review on electrocatalytic coreduction of carbon dioxide and nitrogenous species for urea synthesis, *ACS Nano*, 2023, **17**, 3209–3224.
14 X. Zhang, X. Zhu, S. Bo, C. Chen, M. Qiu, X. Wei, N. He, C. Xie, W. Chen, J. Zheng, P. Chen, S. P. Jiang, Y. Li, Q. Liu

and S. Wang, Identifying and tailoring C–N coupling site for efficient urea synthesis over diatomic Fe–Ni catalyst, *Nat. Commun.*, 2022, **13**, 5337.

15 Y. Pan, C. Zhang, Z. Liu, C. Chen and Y. Li, Structural regulation with atomic-level precision: From single-atomic site to diatomic and atomic interface catalysis, *Matter*, 2020, **2**, 78–110.

16 Q. Hao, H.-X. Zhong, J.-Z. Wang, K.-H. Liu, J.-M. Yan, Z.-H. Ren, N. Zhou, X. Zhao, H. Zhang, D.-X. Liu, L.-W. Chen, J. Luo and X.-B. Zhang, Nickel dual-atom sites for electrochemical carbon dioxide reduction, *Nat. Synth.*, 2022, **1**, 719–728.

17 X. Zhang, X. Zhu, S. Bo, C. Chen, K. Cheng, J. Zheng, S. Li, X. Tu, W. Chen, C. Xie, X. Wei, D. Wang, Y. Liu, P. Chen, S. P. Jiang, Y. Li, Q. Liu, C. Li and S. Wang, Electrocatalytic Urea Synthesis with 63.5% faradaic Efficiency and 100% N-Selectivity via One-step C−N coupling, *Angew. Chem., Int. Ed.*, 2023, **62**(33), e202305447.

18 S. Liu, S. Yin, Z. Wang, Y. Xu, X. Li, L. Wang and H. Wang, AuCu nanofibers for electrosynthesis of urea from carbon dioxide and nitrite, *Cell Rep. Phys. Sci.*, 2022, **3**(5), 100869.

19 J. P. Jones, G. S. Prakash and G. A. Olah, Electrochemical CO2 reduction: recent advances and current trends, *Isr. J. Chem.*, 2014, **54**, 1451–1466.

20 S. Lu, Y. Wang, H. Xiang, H. Lei, B. B. Xu, L. Xing, E. H. Yu and T. X. Liu, Mass transfer effect to electrochemical reduction of CO_2: Electrode, electrocatalyst and electrolyte, *J. Energy Storage*, 2022, **52**, 104764.

21 Y. Wang, H. Li, W. Zhou, X. Zhang, B. Zhang and Y. Yu, Structurally disordered RuO_2 nanosheets with rich oxygen vacancies for enhanced nitrate electroreduction to ammonia, *Angew. Chem., Int. Ed.*, 2022, **61**(19), e202202604.

22 R. M. Arán-Ais, F. Scholten, S. Kunze, R. Rizo and B. Roldan Cuenya, The role of *in situ* generated morphological motifs and Cu(ı) species in C^{2+} product selectivity during CO_2 pulsed electroreduction, *Nat. Energy*, 2020, **5**, 317–325.

23 R. C. DiDomenico and T. Hanrath, Pulse symmetry impacts the C2 product selectivity in pulsed electrochemical CO2 reduction, *ACS Energy Lett.*, 2021, **7**, 292–299.

24 F. Yang, M. J. Kim, M. Brown and B. J. Wiley, Alkaline water electrolysis at 25 A cm− 2 with a microfibrous flow-through electrode, *Adv. Energy Mater.*, 2020, **10**(25), 2001174.

25 C. Kim, L.-C. Weng and A. T. Bell, Impact of pulsed electrochemical reduction of CO2 on the formation of C2+ products over Cu, *ACS Catal.*, 2020, **10**, 12403–12413.

26 J. C. Bui, C. Kim, A. Z. Weber and A. T. Bell, Dynamic boundary layer simulation of pulsed CO2 electrolysis on a copper catalyst, *ACS Energy Lett.*, 2021, **6**, 1181–1188.

27 J. Yan, P. Liu, J. Li, H. Huang and W. Song, Effect of valence state on electrochemical nitrate reduction to ammonia in molybdenum catalysts, *Chem. Eng. J.*, 2023, **459**, 141601.

28 E. Murphy, Y. Liu, I. Matanovic, S. Guo, P. Tieu, Y. Huang, A. Ly, S. Das, I. Zenyuk, X. Pan, E. Spoerke and P. Atanassov, Highly durable and selective Fe-and Mo-based atomically dispersed electrocatalysts for nitrate reduction to ammonia via distinct and synergized NO2–pathways, *ACS Catal.*, 2022, **12**(11), 6651–6662.

29 S. Liu, H. B. Yang, S.-F. Hung, J. Ding, W. Cai, L. Liu, J. Gao, X. Li, X. Ren, Z. Kuang, Y. Huang, T. Zhang and B. Liu, Elucidating the electrocatalytic CO2 reduction reaction over a model single-atom nickel catalyst, *Angew. Chem., Int. Ed.*, 2020, **59**(2), 798–803.

30 Z. Li, D. He, X. Yan, S. Dai, S. Younan, Z. Ke, X. Pan, X. Xiao, H. Wu and J. Gu, Size-dependent nickel-based electrocatalysts for selective CO2 reduction, *Angew. Chem., Int. Ed.*, 2020, **59**(42), 18572–18577.

31 S. Shin, S. Sultan, Z.-X. Chen, H. Lee, H. Choi, T.-U. Wi, C. Park, T. Kim, C. Lee, J. Jeong, H. Shin, T.-H. Kim, H. Ju, H. C. Yoon, H.-K. Song, H.-W. Lee, M.-J. Cheng and Y. Kwon, Copper with an atomic-scale spacing for efficient electrocatalytic co-reduction of carbon dioxide and nitrate to urea, *Energy Environ. Sci.*, 2023, **16**, 2003–2013.

32 J. Liu, X. Guo, T. Frauenheim, Y. Gu and L. Kou, Urea Electrosynthesis Accelerated by Theoretical Simulations, *Adv. Funct. Mater.*, 2024, **34**, 2313420.

33 Y. Luo, K. Xie, P. Ou, C. Lavallais, T. Peng, Z. Chen, Z. Zhang, N. Wang, X.-Y. Li, I. Grigioni, B. Liu, D. Sinton, J. B. Dunn and E. H. Sargent, Selective electrochemical synthesis of urea from nitrate and CO_2 via relay catalysis on hybrid catalysts, *Nat. Catal.*, 2023, **6**, 939–948.

34 A. Han, X. Wang, K. Tang, Z. Zhang, C. Ye, K. Kong, H. Hu, L. Zheng, P. Jiang, C. Zhao, Q. Zhang, D. Wang and Y. Li, An adjacent atomic platinum site enables single-atom iron with high oxygen reduction reaction performance, *Angew. Chem., Int. Ed.*, 2021, **60**(25), 19262–19271.

35 M. Li, H. Zhu, Q. Yuan, T. Li, M. Wang, P. Zhang, Y. Zhao, D. Qin, W. Guo, B. Liu, X. Yang, Y. Liu and Y. Pan, Proximity electronic effect of Ni/Co diatomic sites for synergistic promotion of electrocatalytic oxygen reduction and hydrogen evolution, *Adv. Funct. Mater.*, 2023, **33**(4), 2210867.

36 Z. Zeng, L. Y. Gan, H. B. Yang, X. Su, J. Gao, W. Liu, H. Matsumoto, J. Gong, J. Zhang, W. Cai, Z. Zhang, Y. Yan, B. Liu and P. Chen, Orbital coupling of heterodiatomic nickel-iron site for bifunctional electrocatalysis of CO_2 reduction and oxygen evolution, *Nat. Commun.*, 2021, **12**, 4088.

37 T. Li, S. Ren, C. Zhang, L. Qiao, J. Wu, P. He, J. Lin, Y. Liu, Z. Fu, Q. Zhu, W. Pan, B. Wang and Z. Chen, Cobalt single atom anchored on N-doped carbon nanoboxes as typical single-atom catalysts (SACs) for boosting the overall water splitting, *Chem. Eng. J.*, 2023, **458**, 141435.

38 J.-F. Sun, Q.-Q. Xu, J.-L. Qi, D. Zhou, H.-Y. Zhu and J.-Z. Yin, Isolated single atoms anchored on N-doped carbon materials as a highly efficient catalyst for electrochemical and organic reactions, *ACS Sustainable Chem. Eng.*, 2020, **8**(39), 14630–14656.

39 L. Shan, Y. Ma, S. Xu, M. Zhou, M. He, A. M. Sheveleva, R. Cai, D. Lee, Y. Cheng, B. Tang, B. Han, Y. Chen, L. An, T. Zhou, M. Wilding, A. S. Eggeman, F. Tuna, E. J. L. McInnes, S. J. Day, S. P. Thompson, S. J. Haigh, X. Kang, B. Han, M. Schröder and S. Yang, Efficient electrochemical

reduction of nitrate to ammonia over metal-organic framework single-atom catalysts, *Commun. Mater.*, 2024, **5**, 104.

40 N. Meng, X. Ma, C. Wang, Y. Wang, R. Yang, J. Shao, Y. Huang, Y. Xu, B. Zhang and Y. Yu, Oxide-derived core–shell Cu@ Zn nanowires for urea electrosynthesis from carbon dioxide and nitrate in water, *ACS Nano*, 2022, **16**(6), 9095–9104.

41 I. V. Chernyshova, P. Somasundaran and S. Ponnurangam, On the origin of the elusive first intermediate of CO_2 electroreduction, *Proc. Natl. Acad. Sci. U. S. A.*, 2018, **115**(40), E9261–E9270, DOI: **10.1073/pnas.1802256115**.

42 S. Jiang, K. Klingan, C. Pasquini and H. Dau, New aspects of operando Raman spectroscopy applied to electrochemical CO2 reduction on Cu foams, *J. Chem. Phys.*, 2018, **150**(4), 041718.

43 X. Huang, Y. Li, S. Xie, Q. Zhao, B. Zhang, Z. Zhang, H. Sheng and J. Zhao, The Tandem Nitrate and CO2 Reduction for Urea Electrosynthesis: Role of Surface N-Intermediates in CO2 Capture and Activation, *Angew. Chem., Int. Ed.*, 2024, **63**(24), e202403980.

44 J. Xian, *et al.*, Electrosynthesis of α-Amino Acids from NO and other NOx species over CoFe alloy-decorated Self-standing Carbon Fiber Membranes, *Angew. Chem., Int. Ed.*, 2023, **135**(30), e202306726.

45 M. Muhyuddin, G. Zuccante, P. Mustarelli, J. Filippi, A. Lavacchi, L. Elbaz, Y.-H. Chen, P. Atanassov and C. Santoro, Electrochemical urea production using carbon dioxide and nitrate: state of the art and perspectives, *Energy Environ. Sci.*, 2024, **17**, 3739–3752.

46 X. Zhang, X. Zhu, S. Bo, C. Chen, M. Qiu, X. Wei, N. He, C. Xie, W. Chen, J. Zheng, P. Chen, S. P. Jiang, Y. Li, Q. Liu and S. Wang, Identifying and tailoring C–N coupling site for efficient urea synthesis over diatomic Fe–Ni catalyst, *Nat. Commun.*, 2022, **13**, 5337.